Title

Casting Nanoporous Platinum in Metal—Organic Frameworks

Journal

Advanced Materials, 31(12)

ISSN

0935-9648

Authors

Gao, Xiang

Pei, Xiaokun

Gardner, David W

et al.

Publication Date

2019-03-01

DOI

10.1002/adma.201807553

Peer reviewed

DOI: 10.1002/adma.201807553

Article type: Communication

Casting Nanoporous Platinum in Metal-Organic Frameworks

*Xiang Gao, Xiaokun Pei, David W. Gardner, Christian S. Diercks, Seungkyu Lee, Bunyarat Rungtaweevoranit, Mathieu Prevot, Chenhui Zhu, Sirine Fakra, Roya Maboudian**

X. Gao, X. Pei, Dr. C. Diercks, Dr. S. Lee, Dr. B. Rungtaweevoranit, Dr. M. Prevot
Department of Chemistry
University of California, Berkeley, California 94720, USA

D. Gardner, Prof. R. Maboudian
Department of Chemical & Biomolecular Engineering
University of California, Berkeley, California 94720, USA
Email: maboudia@berkeley.edu

Dr. C. Zhu, Dr. S. Fakra
Advanced Light Source
Lawrence Berkeley National Laboratory, Berkeley, California 94720, USA

Keywords: nanocasting, metal-organic frameworks, nanoporous platinum, methanol electrooxidation reaction

Nanocasting based on porous templates is a powerful strategy in accessing materials and structures that are difficult to form by the bottom-up syntheses in a controlled fashion. Here, we report a facile synthetic strategy for casting ordered, nanoporous platinum (NP-Pt) networks with a high degree of control by using metal-organic frameworks (MOFs) as templates. The Pt precursor was first infiltrated into zirconium-based MOFs and subsequently transformed to 3D metallic networks via a chemical reduction process. We demonstrate that the dimensions and topologies of the casted

NP-Pt networks can be accurately controlled by using different MOFs as templates. The Brunauer−Emmett−Teller (BET) surface areas of the NP-Pt networks are estimated to be > 100 m^2/g and they exhibit excellent catalytic activities in the methanol electrooxidation reaction (MEOR). This new methodology presents an attractive route to prepare well-defined nanoporous materials for diverse applications ranging from energy to sensing and biotechnology.

Introduction

Nanocasting is a synthetic process in which precursors are solidified in the replica phases of templates to afford self-standing porous structures.[1] This strategy is powerful for creating nanoporous materials that are difficult to synthesize by the conventional bottom-up processes.[2] Specifically, nanocasting has been explored for the syntheses of nanoporous metals,[3] metal oxides,[4] carbon,[5] and other inorganic materials.[6] A long-standing objective in this context is to design well-defined structures that serve as templates for constructing porous 3D architectures with a high level of precision.[7–9] Traditionally, porous silica,[10,11] lyotropic liquid crystals,[12,13] and nanospheres assemblies[14,15] have been employed in this process. However, the amorphous backbones of these materials intrinsically inhibit the design of structures with molecular accuracy, and the casted phases are limited to low surface areas. More structurally defined crystalline zeolites have been shown to function as templates for casting highly porous carbon with controlled structures;[16,17] however, introducing metals or metal oxides into

zeolites generally leads to the formation of isolated particles instead of extended porous networks.[18,19] As such, developing effective templates for casting nanoporous materials with tunable and controllable structures remains a significant challenge.

Metal-organic frameworks (MOFs) are a class of nanoporous crystalline materials with well-defined structures and high surface areas.[20–22] MOFs are ideally suited as templates for nanocasting process because of their high porosities, accessible interconnected pore structures, and crystalline backbones. Due to the modular construction based on the discrete polynuclear inorganic clusters (secondary building units, SBUs) and organic linkers, the structure type (topology) and metrics of MOFs can be tailored to achieve the desired pore size and surface area.[23,24] While syntheses of nanoporous carbon[25] and metal oxides[26,27] within MOF-templates have been reported, in both cases the replica phases show ill-defined structures with poor ordering. More recently, it was reported that ultrathin, well-aligned metallic nanowires can be uniformly casted into zirconium-based MOF-545,[28] where the MOF's one-dimensional channels are critical for confining the growth of the nanowires. However, casting ordered and porous 3D nanostructures in MOFs still remains an outstanding challenge.

The difficulty of using MOFs as templates for nanocasting lies in controlling the process such that casting occurs exclusively inside of the internal void space instead of aggregation on the external surface of the crystal.[29–32] In

this report we demonstrate that metallic Pt structures can be effectively casted into zirconium-based MOFs by a two-step infiltration/reduction process. Upon removal of the MOF template, nanoporous Pt networks (NP-Pt) with periodic order and high internal surface areas are obtained. We show that the key to avoiding aggregation on MOFs is to cast the Pt selectively into the continuous channels but not within spatially isolated pores. Tailoring the structure types and pore metrics of MOF templates directly translates to the formation of nanoporous platinum networks of different topologies and with the highest reported internal surface areas for platinum known to date. The casted NP-Pt networks exhibit excellent catalytic activities for methanol electrooxidation and the performance of different NP-Pt networks show a direct correlation between the materials' surface area and catalytic performance.

Results and Discussion

As the first demonstration of nanocasting 3D metal structures within MOFs, we chose the Zr(IV) based MOF-808 for its capability of anchoring metal atoms onto the SBUs. We hypothesized that such metal species can serve as nucleation sites for the subsequent growth of an extended 3D nanoporous metal network.[33] In MOF-808, each 6-connected (6-c) Zr_6-SBU is linked to six 1,3,5-benzenetricarboxylate (BTC) linkers to form a 3D porous framework containing two different types of pores (open channels with aperture diameters of 16 Å, **Scheme 1**a).[34,35] A microcrystalline powder of MOF-808 was treated with dilute HCl to remove capping formates and provide

accessible binding sites (OH^-/H_2O groups) to anchor metal ions. Placing HCl-treated MOF-808 into an aqueous solution of potassium tetrachloroplatinate (K_2PtCl_4) affords MOF-808-Pt, where the introduced OH^-/H_2O groups bind to platinum in a chelating mode (Supporting Information, SI, Section S1).[33] The crystallinity and porosity of MOF-808-Pt were retained as determined by powder X-ray diffraction (PXRD) of the material as well as its N_2 adsorption isotherm, respectively (Figures S10 and S28). Inductively coupled plasma atomic emission spectroscopy (ICP-AES) analysis demonstrated the presence of platinum in MOF-808-Pt (Table S4). The infrared spectroscopy upon CO adsorption showed a C-O stretching band at 2110 cm^{-1} on MOF-808-Pt, corroborating the existence of single Pt^{2+} ions in the structure which can bind to CO molecules (Figure S1).[36] Scanning electron microscopy (SEM) was applied to demonstrate the retained morphology of MOF-808-Pt (Figure S23), and the elemental phase mapping of MOF-808-Pt indicated the uniform distribution of Pt throughout the whole MOF crystals (Figure S13).

X-ray diffraction of the MOF-808-Pt single crystal (SI, Section S3) provided unequivocal evidence for oxygen-bound Pt species inside of the MOF. Two types of cr[illegible] site[illegible] both of which Pt is [illegible]s of [illegible]g mode (Figures S2[illegible]tructu[illegible]d strong coordinative [illegible] the P[illegible] Scheme 1c). It was observed that Pt atoms were exclusively localized in the adaman[illegible] d no Pt at[illegible] isolated

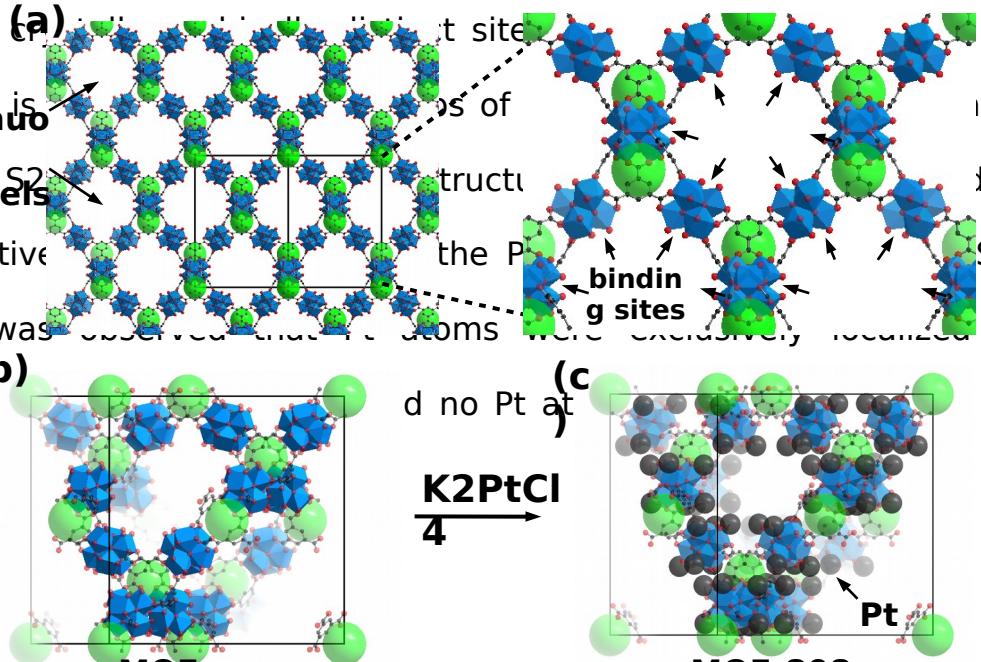

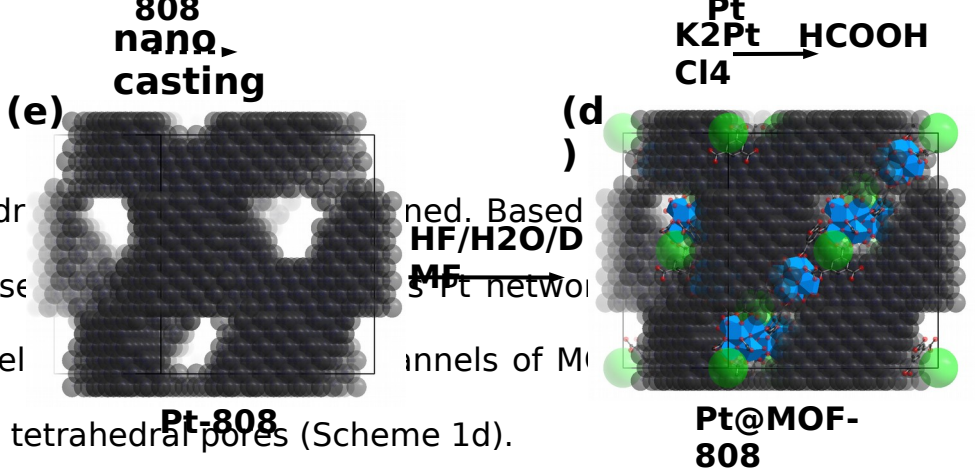

tetrahedr ned. Based cted that the subse s Pt netwo e casted selectivel nnels of M ithin the isolated tetrahedral pores (Scheme 1d).

Scheme 1. (a) Crystal structure of MOF-808 contains large interconnected channels (open space) and isolated tetrahedral pores (green spheres). 6-c Zr_6-SBUs provide binding sites for anchoring metal precursors. (b-e)

Illustration of the process of nanocasting Pt metal within the MOF-808-template. (b) Unit cell of MOF-808. (c) Unit cell of MOF-808-Pt with the infiltrated Pt precursor. (d) Simulated unit cell of Pt@MOF-808 after the reduction of Pt precursor. (e) Simulated unit cell of NP-Pt-808 after etching of the MOF-808 template.

The formation of the metallic Pt phase in MOF-808 (Pt@MOF-808) was realized by adding HCOOH as the reducing agent (Scheme 1c to 1d). HCOOH reduces Pt^{2+} to Pt^0, and it is in turn oxidized to CO_2.[37] K_2PtCl_4 and HCOOH were added sequentially into an aqueous dispersion of MOF-808-Pt to afford Pt@MOF-808. The formation of CO_2 and the change in color of the dispersion (pale pink to black) indicated the proceeding of the expected reaction (Figure S4). The reduction of Pt precursor was further verified by X-ray absorption near-edge structure (XANES) spectroscopy of the etched sample without MOF-template (Figure S12). PXRD of Pt@MOF-808 powders showed similar diffraction patterns as the parent MOF-808-Pt (Figure S10), indicating the integrity of the MOF structure throughout the casting process. The N_2 adsorption isotherm of the activated Pt@MOF-808 powders displayed a drastic loss of porosity which is attributed to the pores of MOF-808 being occupied by Pt during the casting process (Figure S28).

The crystals of Pt@MOF-808 retained its single-crystallinity, thus allowing for the structure of MOF-808 to be solved by X-ray diffraction (SI, Section S3). The crystallographic analysis of the diffraction patterns with noticeably larger mosaicity indicated an fcc packing of Pt atoms (Figure S5). Based on the

precision images, the respective orientation of the unit cells for MOF-808 and the incorporated fcc packed Pt overlapped perfectly. However, efforts to solve the atomic structure at the interface between the casted Pt phase and MOF-808 were not successful due to large disorder of the guest species within the pores.

The MOF template of Pt@MOF-808 was chemically etched by hydrofluoric acid (SI, Section S1). Following the digestion, the material was washed with acetone to afford Pt-808 as black powders. It was found that the particle size of Pt-808 could be tuned from 800 to 40 nm by changing the amount of reagents added in the reaction (Figures S14). Specifically, the addition of ethylene glycol effectively decreased the particle size during the casting process.[38] Elemental and ICP-AES analyses of Pt-808 powders indicated that the etched sample consisted predominately of pure metallic Pt (Table S5), which is consistent with the result obtained from XANES. The structure of Pt-808 was simulated based on the hypothesis that Pt occupying the continuous adamantane-shaped channels remained interconnected after chemical etching, and the porosity of Pt-808 originates from the space provided by the MOF-808 backbone (Figures S7 and S8). The crystal unit cell of the modeled structure was determined as *F*$\acute{4}$3m with a = 35.2 Å, and the network was assigned to possess a diamond (**dia**) topology. The Pt atoms of Pt-808 are arranged in an fcc packing mode, which is experimentally confirmed by X-ray diffraction data (Figure S5).

A direct evidence for the templating effect of MOF-808 in nanocasting was obtained based on SEM images. The similarities in the appearance of MOF-808 and Pt-808 (800 nm) (**Figure 1**a and S22-24) indicate that the Pt-808 (800 nm) particles adopt the morphology of their MOF-808 progenitor during the casting process. Transmission electron microscopy (TEM) images of Pt-808 displayed solid contrasts in bodies of particles (Figures 1c and S16), which suggest that the reduction of the Pt precursor occurred largely at the internal surfaces of MOF-808 instead of at the external surface of the crystals. SEM and TEM images of the smaller Pt-808 particles (average sizes: 200 and 40 nm, Figures S15) showed that Pt-808 particles were isolated from each other and possessed narrow particle size distributions. Interestingly, some Pt-808 (200 nm) particles showed octahedral morphologies (Figures 1b, 1d, and S16) which are commensurate with the cubic $m\bar{3}m$ group symmetry.[39] This result additionally implies that the casted Pt particles originated from MOF-808 as the template, which possesses cubic symmetry space group as well ($Fd\bar{3}m$).

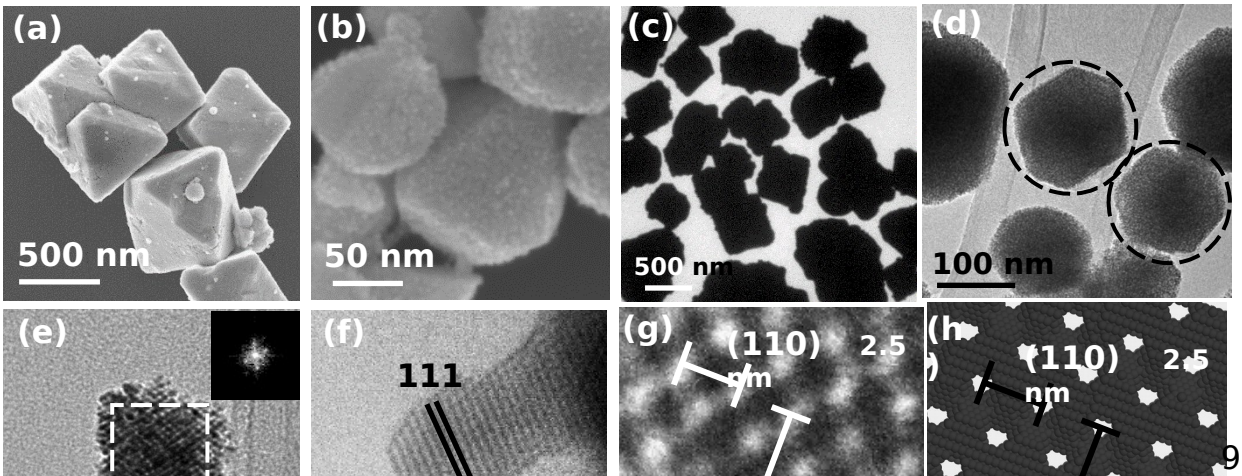

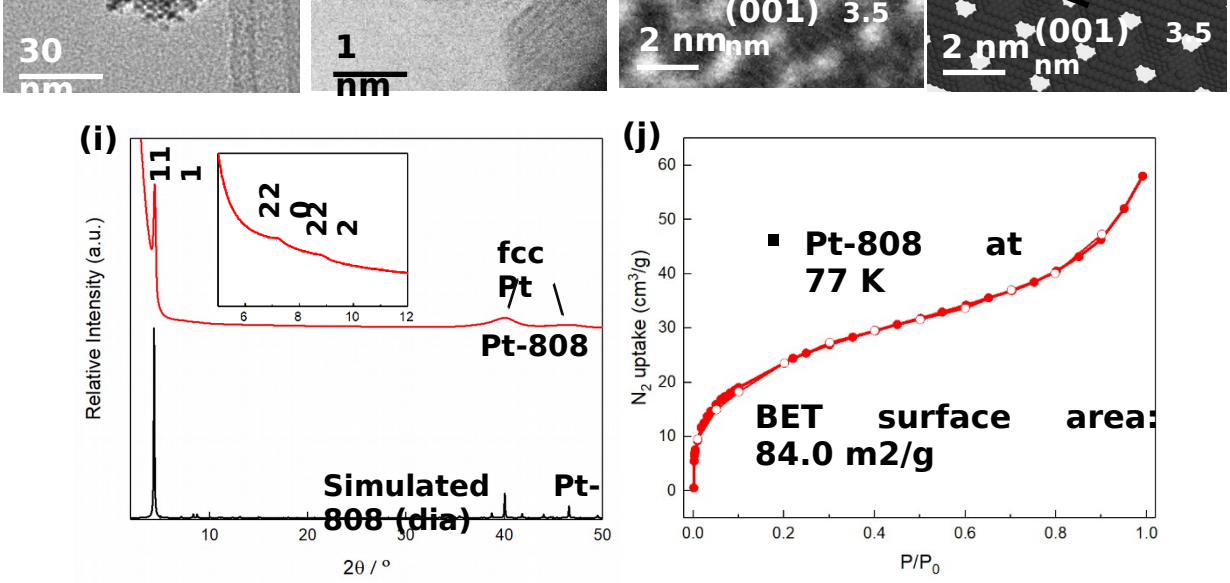

Figure 1. SEM images of (a) Pt-808 (800 nm) and (b) Pt-808 (200 nm). TEM images of (c) Pt-808 (800 nm) and (d) Pt-808 (200 nm); octahedron-shaped particles are circled by dashed lines. (e, f) TEM and HRTEM images, respectively, of Pt-808 (40 nm). The inset in figure (e) is the fast fourier transform (FFT) pattern of the selected region. (g) Magnified TEM image of Pt-808 (40 nm). (h) Simulated structure of Pt-808 viewed along the <110> axis. (i) Comparison of the 1D line-profile of SAXS/WAXS for Pt-808 (200 nm) with the simulated pattern based on the modeled structure (**dia** topology). (j) N_2 adsorption isotherm of Pt-808 (200 nm) particles.

Due to the smaller particle size of Pt-808 (40 nm), its TEM image displayed porous lattices with spatial ordering (Figure 1e). As magnified in Figure 1g, the periodic matrix was observed in Pt-808, which is consistent with the

modeled structure viewed along the <110> axis (Figures 1h and S8). Specifically, the spacings for the (110) and (001) lattice planes in Pt-808 matched well with the values calculated from the simulated structure, corroborating that the structure of Pt-808 particles corresponds to an inversion replica of MOF-808 (SI, Section S4). High-resolution TEM (HRTEM) on the edges of Pt-808 particles showed clear lattice fringes, which correspond to the (111) crystal planes in fcc packing of Pt atoms (Figure 1f).

The crystalline characteristics of Pt-808 particles were further evaluated by small/wide angle X-ray scattering measurement (SAXS/WAXS) (Figure 1i). The SAXS/WAXS pattern for Pt-808 (200 nm) was found to be in good agreement with the simulated structure, confirming the templating effect of MOF-808. The broad peaks at high angles were assigned to the 111 and 200 reflections of the fcc packing of Pt atoms. Permanent porosity of the Pt-808 powder was verified by N_2 adsorption (Figure 1j) and the BET surface area of Pt-808 (200 nm) was estimated to be 84.0 $m^2\ g^{-1}$ (Figure S30). Compared to the porous platinum prepared by other templates,[40,41] the MOF-templated Pt-808 provides superior porosity and higher internal surface area.

The building units of MOFs can be systematically tuned by adjusting their dimensions to tailor the pore metrics of a given structure while retaining the structure type of the parent framework — a strategy commonly referred to as the isoreticular principle.[23,24] Making use of this strategy PCN-777 was chosen as the template to synthesize NP-Pt networks as well. The crystal

structure of PCN-777 is constructed from connecting 6-c Zr_6-SBUs and 4,4′,4′′-s-triazine-2,4,6-triyl-tri-benzoate (TATB) linkers and the framework has the same underlying topology as MOF-808 (**Scheme 2**).[42] However, compared to MOF-808, PCN-777 possesses larger pores and wider channels (with aperture diameters of 32 Å) imparted by the expansion of its organic building blocks. Nanocasting of NP-Pt in PCN-777 was carried out under the same condition as outlined for Pt-808, and the obtained NP-Pt powder was designated as Pt-777.

The topological structure of Pt-777 was simulated based on the principles applied for Pt-808, and the crystallinity of the obtained powder was confirmed by X-ray scattering measurement (**Figure 2**c). Compared to the SAXS/WAXS pattern of Pt-808, the (111) scattering peak of Pt-777 was shifted to a lower angle, in agreement with the predicted structural expansion (Inset in Figure 2c). The TEM and HAADF-STEM images of Pt-777 particles displayed ordered porous lattices (Figures 2a and 2b) and are consistent with the simulated structure. The spacings of the (110) and (001) lattice planes in Pt-777 particles were determined to be 3.9 and 5.6 nm based on TEM images, respectively, in accordance with the data obtained from SAXS/WAXS results. Measurement of the N_2 adsorption isotherm for Pt-777 powder confirmed its permanent porosity, and the BET surface area was calculated to be 103.1 $m^2\ g^{-1}$ (Figures 2g and S30).

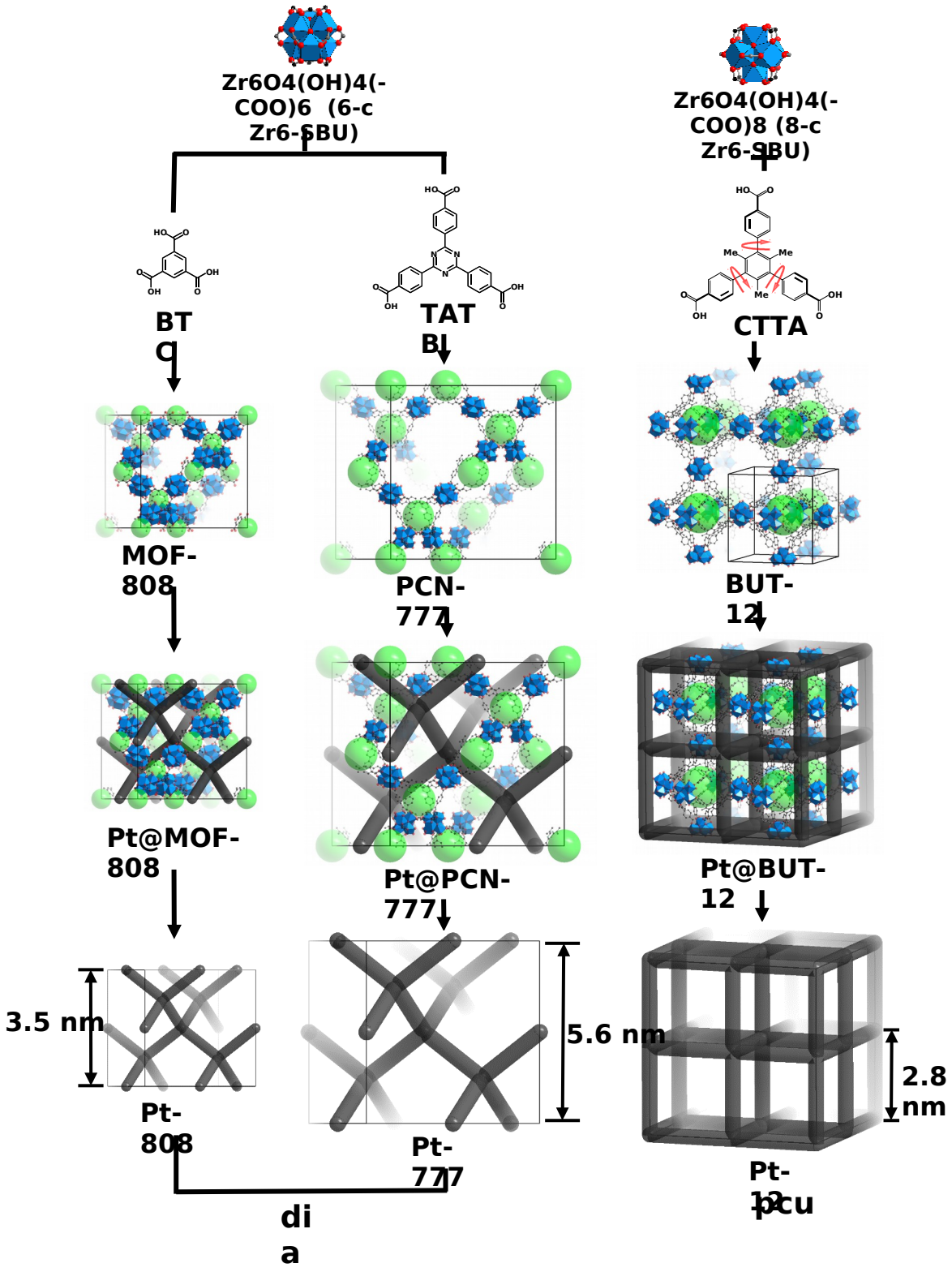

Scheme 2. Illustration of nanocasting NP-Pt networks in MOF-808, PCN-777, and BUT-12 with tunable metrics and structure types. The isolated pores in

MOFs are represented by green spheres.

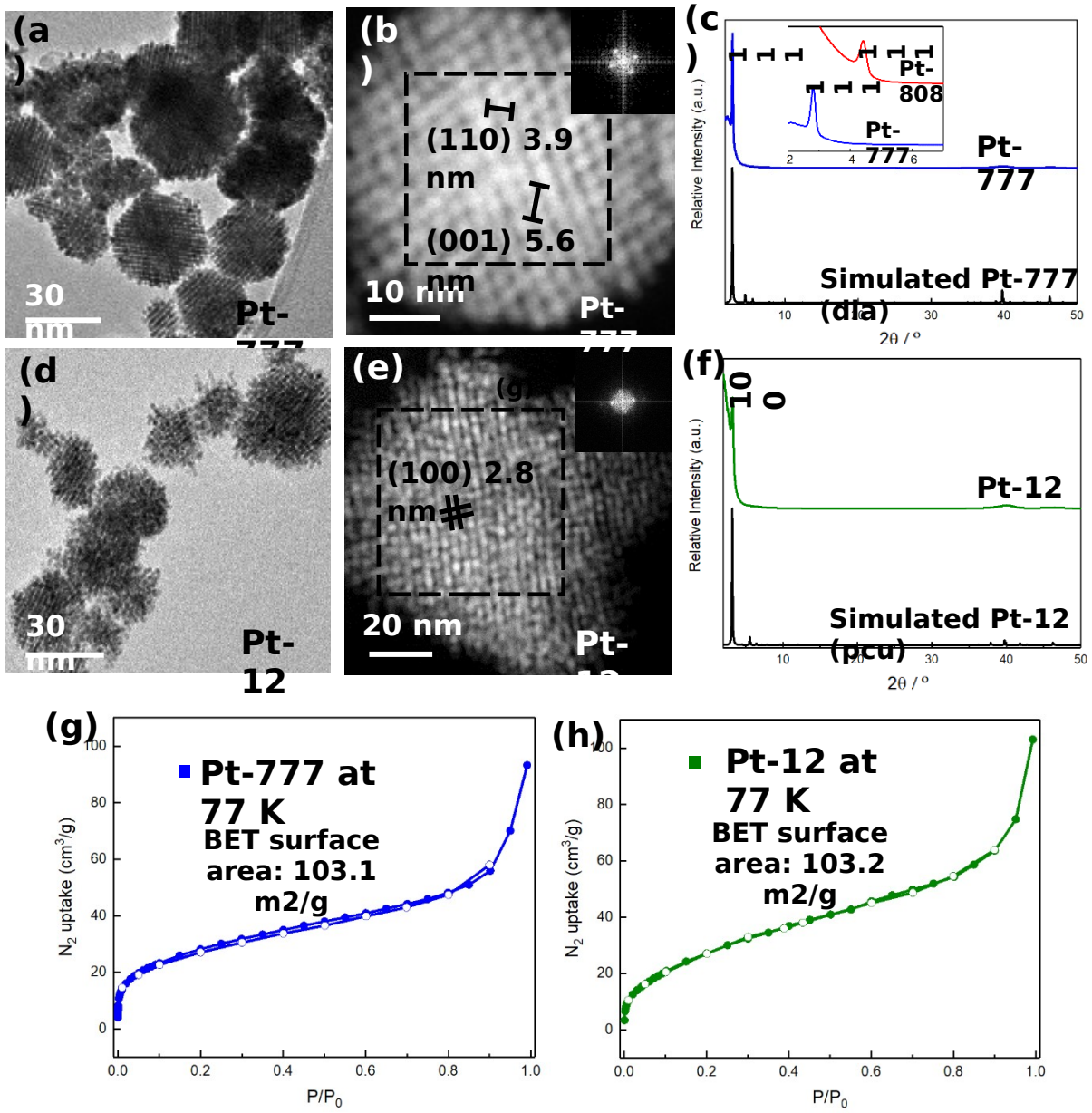

Figure 2. TEM images of (a) Pt-777, and (d) Pt-12. HAADF-STEM images of (b) Pt-777, and (e) Pt-12. The insets are FFT patterns of the selected regions. (c) Comparison of the 1D line-profile of SAXS/WAXS for Pt-777 with the simulated pattern based on the modeled structure (**dia** topology). The inset is the comparison of SAXS/WAXS patterns for Pt-777 and Pt-808. (f)

Comparison of 1D line-profile of SAXS/WAXS for Pt-12 with the simulated pattern based on based on the modeled structure (**pcu** topology). (g, h) N_2 adsorption isotherm of Pt-777 and Pt-12 particles, respectively.

In addition to the isoreticular expansion, the structure type of MOFs can be designed through the judicious choice of building blocks.[42] The introduction of methyl groups in 5′-(4-carboxyphenyl)-2′,4′,6′-trimethyl-[1,1′:3′,1″-terphenyl]-4,4″-dicarboxylic acid (CTTA) affords a tritopic building unit with carboxylate groups oriented perpendicular to the central benzene ring. Due to the different orientation of the terminal binding groups, the combination of CTTA linkers with 8-c Zr_6-SBUs yields a framework with **the-a** topology, termed BUT-12.[43] The structure of BUT-12 contains two different types of pores: (i) Smaller octahedral pores which are isolated from each other and (ii) larger cuboctahedron-shaped pores which are interconnected to form continuous channels (Scheme 2). Pt-12 was synthesized and its structure was characterized based on the same principles applied for Pt-808 and Pt-777. Since in BUT-12 the isolated octahedral pores do not interact with the Pt precursor due to the lack of binding sites,[44] the spatial distribution of the Pt network is proposed to be located exclusively inside the cuboctahedron-shaped channels of BUT-12 (Scheme 2). The unit cell of the simulated structure for Pt-12 was determined as *P*m$\bar{3}$m with a = 28.3 Å, and the topology was assigned as primitive cubic (**pcu**). Structural information of the models for Pt-808, Pt-777, and Pt-12 is summarized in Table S3.

The SAXS/WAXS pattern of Pt-12 powder confirmed its ordered structure within the BUT-12 template (Figure 2f). TEM and HAADF-STEM analyses demonstrated that Pt-12 particles possess a rectangular lattice pattern which matches the projection of a network with **pcu** topology (Figures 2d and S18). The spacing of the (100) lattice plane in Pt-12 particles was estimated to be 2.8 nm (Figure 2e), which is identical to the value calculated based on the modeled structure (Scheme 2). N_2 adsorption of Pt-12 confirmed the permanent porosity of the structure, and the BET surface area was estimated to be 103.2 m^2/g (Figure 2h and S30). As such, the surface areas of Pt-12 and Pt-777 constitute the highest value reported for porous Pt to date.[39]

Due to the high surface areas of the NP-Pt particles casted from MOF-templates, we benchmarked the electrocatalytic performance of Pt-808, Pt-777, and Pt-12 against commercial Pt black catalyst in the methanol electrooxidation reaction (MEOR). The particle sizes of the casted NP-Pt networks were first optimized to approximately 35-40 nm to minimize the mass transfer resistance in electrocatalysis. The surface morphology of thin films prepared by drop casting NP-Pts on electrodes were characterized by SEM. Figure S25 shows the homogeneous dispersions of Pt-808, Pt-777 and Pt-12 particles on the substrates. The electrocatalytic performance of Pt catalysts recorded in an aqueous solution of methanol is displayed in **Figure 3**. Two anodic peaks occurring on the positive and negative sweeps, typical features in MEOR, were observed for all Pt catalysts. The mass activities and specific activities were calculated by normalizing the MEOR current density

with the corresponding loading amount of platinum and the electrochemical surface areas (ECSAs) of Pt black and NP-Pt samples, respectively (SI, Section S11).

As shown in Figure 3a, the mass activity of Pt-808 at 0.7 V (0.525 A mg^{-1}) is much higher than that of Pt black (0.145 A mg^{-1}). By comparing the mass activities among Pt-808, Pt-777, and Pt-12, we found that Pt-12 particles exhi 1.76 mA .8 e of comi 3c set pote cle tive valu dat ials. [45,46] ord OF- temp as comp of the p he chara in Figur rm large ter

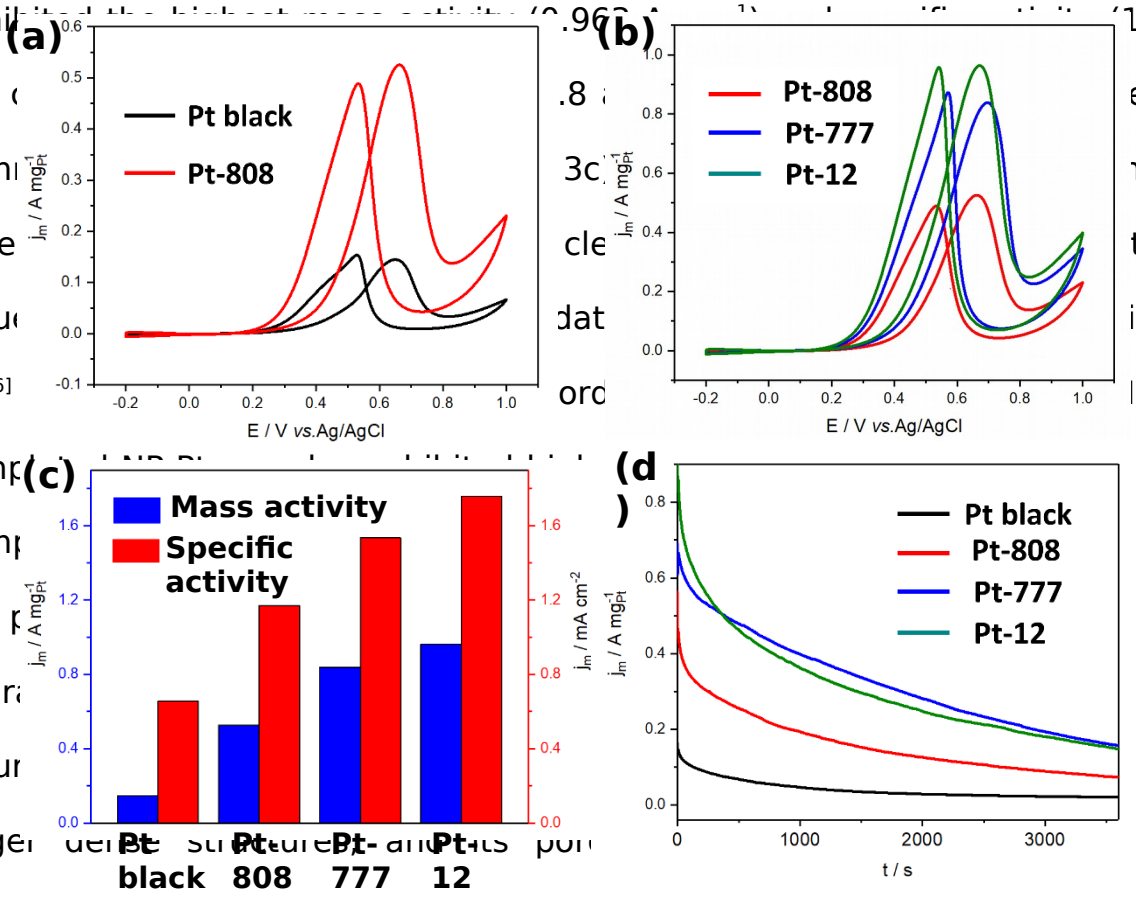

catalysis. A summary of the catalytic performance of the NP-Pt catalysts and benchmarking against commercial Pt black is given in Table S6.

Figure 3. Cyclic voltammograms of MEOR for Pt black and MOF-templated NP-Pts. Scan rate is 50 mV/s. (a) Comparison of MEOR mass activity for Pt-808 and Pt black. (b) Comparison of MEOR mass activities for Pt-808, Pt-777, and Pt-12. (c) Histograms of the mass activities and specific activities for all four catalysts at 0.7 V. (d) Current−time curves of Pt catalysts recorded at 0.6 V.

To explore the generality of MOF-templated nanocasting for nanoporous metals, the syntheses of rhodium (Rh), palladium (Pd), and Pt-based alloys (Pt_xPd_{1-x}, Pt_yRh_{1-y}) with the different composition were conducted using the MOF-808 template. The casted samples were characterized by TEM (Figures S19 and S20) to demonstrate the presence of accessible pores. MEOR experiments of the obtained nanoporous Pt-alloys showed catalytic activities comparable to that of Pt-808 catalyst (Figure S33). We hypothesize that the

high surface areas along with the large degree of curvatures imparted by the MOF template significantly contribute to the excellent activities of the casted NP-Pt catalysts.[47] Since the surface morphology and the coordination environment drastically impact the activity of Pt-based catalysts in electrocatalytic processes[48,49] a more detailed characterization of the surface structure of the casted NP-Pts is needed for the mechanistic insight into the observed electrocatalytic performance. These studies are the current focus of our research.

Conclusion

In summary, we have demonstrated that ordered, nanoporous platinum networks with controlled structures can be accurately casted using MOF-templates. For the first time, precise nanocasting was achieved in well-defined platforms with the designable dimensions and structure types. Based on the results obtained by X-ray diffraction, X-ray scattering, and electron microscopy, we confirmed that nanocasting in MOFs can be achieved by selectively controlling the formation of the casted phase within continuous interconnected channels as opposed to the isolated pores of frameworks. Compared to traditional casting templates, the molecularly defined and rationally designed structures of MOFs as well as their high porosities and surface areas render them ideal scaffolds for the formation of nanoporous metal networks with an unprecedented level of control over the metal's structure type and pore metrics. Inspired by the large structural diversity of

MOFs with varied pore environments and topologies, we expect the approach reported in here to be applicable to a vast variety of MOF-templated nanostructures.

Supporting Information

Supporting Information is available from the Wiley Online Library or from the author.

Acknowledgements

Support for the synthesis by King Abdulaziz City for Science and Technology (Center of Excellence for Nanomaterials and Clean Energy Applications). The single-crystal X-ray diffraction data was collected at beamline 11.3.1, Advanced Light Source, Lawrence Berkeley National Laboratory, which is supported by the Director, Office of Science, Office of Basic Energy Sciences, of the U.S. Department of Energy under Contract No. DE-AC02-05CH11231. X. G. acknowledges Dr. E. Kapustin and Dr. J. Yang for synchrotron X-ray diffraction data acquisition support, Dr. H. Liu, Dr. Y. Ma, and Dr. C. Xie for TEM acquisition, and Dr. H. Frei and Dr. G. Katsoukis for CO FT-IR acquisition.

References

[1] H. Yang, D. Zhao, *J. Mater. Chem.* **2005**, *15*, 1217.

[2] A. H. Lu, F. Schüth, *Adv. Mater.* **2006**, *18*, 1793.

[3] Y. J. Han, J. M. Kim, G. D. Stucky, *Chem. Mater.* **2000**, *12*, 2068.

[4] P. Yang, D. Zhao, D. I. Margolese, B. F. Chmelka, G. D. Stucky, *Nature* **1998**, *396*, 152.

[5] R. Ryoo, S. H. Joo, S. Jun, *J. Phys. Chem. B* **1999**, *103*, 7743.

[6] F. Gao, Q. Lu, D. Zhao, *Adv. Mater.* **2003**, *15*, 739.

[7] M. E. Davis, *Nature* **2002**, *417*, 813.

[8] Q. Huo, D. I. Margolese, U. Ciesla, P. Feng, T. E. Gier, P. Sieger, R. Leon, P. M. Petroff, F. Schüth, G. D. Stucky, *Nature* **1994**, *368*, 317.

[9] K. Na, C. Jo, J. Kim, K. Cho, J. Jung, Y. Seo, R. J. Messinger, B. F. Chmelka, R. Ryoo, *Science* **2011**, *333*, 328.

[10] X. Deng, K. Chen, H. Tüysüz, *Chem. Mater.* **2017**, *29*, 40.

[11] S. Jun, Sang Hoon Joo, R. Ryoo, M. Kruk, M. Jaroniec, Z. Liu, T. Ohsuna, O. Terasaki, *J. Am. Chem. Soc.* **2000**, *122*, 10712.

[12] J. S. Beck, J. C. Vartuli, W. J. Roth, M. E. Leonowicz, C. T. Kresge, K. D. Schmitt, C. T. W. Chu, D. H. Olson, E. W. Sheppard, S. B. McCullen, J. B. Higgins, J. L. Schlenker, *J. Am. Chem. Soc.* **1992**, *114*, 10834.

[13] G. S. Attard, P. N. Bartlett, N. R. B. Coleman, J. M. Elliott, J. R. Owen, J. Wang, *Science* **1997**, *278*, 838.

[14] E. J. W. Crossland, N. Noel, V. Sivaram, T. Leijtens, J. A. Alexander-Webber, H. J. Snaith, *Nature* **2013**, *495*, 215.

[15] Y. Song, W. Yin, Y. H. Wang, J. P. Zhang, Y. Wang, R. Wang, J. Han, W. Wang, S. V. Nair, H. E. Ruda, *Sci. Rep.* **2014**, *4*, 30.

[16] K. Kim, T. Lee, Y. Kwon, Y. Seo, J. Song, J. K. Park, H. Lee, J. Y. Park, H. Ihee, S. J. Cho, R. Ryoo, *Nature* **2016**, *535*, 131.

[17] Z. Yang, Y. Xia, R. Mokaya, *J. Am. Chem. Soc.* **2007**, *129*, 1673.

[18] L. Liu, U. Díaz, R. Arenal, G. Agostini, P. Concepción, A. Corma, *Nat.*

Mater. **2017**, *16*, 132.

[19] W. M. H. Sachtler, *Acc. Chem. Res.* **1993**, *26*, 383.

[20] H. Li, M. Eddaoudi, M. O'Keeffe, O. M. Yaghi, *Nature* **1999**, *402*, 276.

[21] S. Kitagawa, R. Kitaura, S. I. Noro, *Angew. Chem., Int. Ed.* **2004**, *43*, 2334.

[22] H. Furukawa, K. E. Cordova, M. O'Keeffe, O. M. Yaghi, *Science* **2013**, *341*.1230444

[23] H. Deng, S. Grunder, K. E. Cordova, C. Valente, H. Furukawa, M. Hmadeh, F. Gándara, A. C. Whalley, S. A. Z. Liu, H. Kazumori, M. O'Keeffe, O. Terasaki, J. F. Stoddart, O. M. Yaghi, *Science* **2012**, *338*, 1321.

[24] M. Eddaoudi, J. Kim, N. Rosi, D. Vodak, J. Wachter, M. O. Keeffe, O. M. Yaghi, *Science* **2002**, *295*, 469.

[25] B. Liu, H. Shioyama, T. Akita, Q. Xu, *J. Am. Chem. Soc.* **2008**, *130*, 5390.

[26] A. S. Hall, A. Kondo, K. Maeda, T. E. Mallouk, *J. Am. Chem. Soc.* **2013**, *135*, 16276.

[27] C. D. Malonzo, Z. Wang, J. Duan, W. Zhao, T. E. Webber, Z. Li, I. S. Kim, A. Kumar, A. Bhan, A. E. Platero-Prats, K. W. Chapman, O. K. Farha, J. T. Hupp, A. B. F. Martinson, R. L. Penn, A. Stein, *Inorg. Chem.* **2018**, *57*, 2782.

[28] B. Volosskiy, K. Niwa, Y. Chen, Z. Zhao, N. O. Weiss, X. Zhong, M. Ding, C. Lee, Y. Huang, X. Duan, *ACS Nano* **2015**, *9*, 3044.

[29] N. Tsumori, L. Chen, Q. Wang, Q. L. Zhu, M. Kitta, Q. Xu, *Chem* **2018**, *4*,

845.

[30] F. R. Fortea-Pérez, M. Mon, J. Ferrando-Soria, M. Boronat, A. Leyva-Pérez, A. Corma, J. M. Herrera, D. Osadchii, J. Gascon, D. Armentano, E. Pardo, *Nat. Mater.* **2017**, *16*, 760.

[31] H. L. Jiang, Q. P. Lin, T. Akita, B. Liu, H. Ohashi, H. Oji, T. Honma, T. Takei, M. Haruta, Q. Xu, *Chem. Eur. J.* **2011**, *17*, 78.

[32] A. Aijaz, A. Karkamkar, Y. J. Choi, N. Tsumori, E. Rönnebro, T. Autrey, H. Shioyama, Q. Xu, *J. Am. Chem. Soc.* **2012**, *134*, 13926.

[33] K. Otake, Y. Cui, C. T. Buru, Z. Li, J. T. Hupp, O. K. Farha, *J. Am. Chem. Soc.* **2018**, *140*, 8652.

[34] H. Furukawa, F. Gándara, Y.-B. Zhang, J. Jiang, W. L. Queen, M. R. Hudson, O. M. Yaghi, *J. Am. Chem. Soc.* **2014**, *136*, 4369.

[35] J. Jiang, F. Gándara, Y. B. Zhang, K. Na, O. M. Yaghi, W. G. Klemperer, *J. Am. Chem. Soc.* **2014**, *136*, 12844.

[36] L. M. Kustov, D. Ostgard, W. M. H. Sachtler, *Catal. Letters* **1991**, *9*, 121.

[37] S. Schuldiner, B. Piersma, *J. Catal.* **1969**, 13, *413*.

[38] F. Bonet, C. Guery, D. Guyomard, R. H. Urbina, K. Tekaia-Elhsissen, J. M. Tarascon, *Int. J. Inorg. Mater.* **1999**, *1*, 47.

[39] H. Wang, H. Y. Jeong, M. Imura, L. Wang, L. Radhakrishnan, N. Fujita, T. Castle, O. Terasaki, Y. Yamauchi, *J. Am. Chem. Soc.* **2011**, *133*, 14526.

[40] Y. Doi, A. Takai, Y. Sakamoto, O. Terasaki, Y. Yamauchi, K. Kuroda, *Chem. Commun.* **2010**, *46*, 6365.

[41] S. Akbar, J. M. Elliott, M. Rittman, A. M. Squires, *Adv. Mater.* **2013**, *25*,

1160.

[42] D. Feng, K. Wang, J. Su, T. F. Liu, J. Park, Z. Wei, M. Bosch, A. Yakovenko, X. Zou, H. C. Zhou, *Angew. Chem., Int. Ed.* **2015**, *54*, 149.

[43] B. Wang, X. L. Lv, D. Feng, L. H. Xie, J. Zhang, M. Li, Y. Xie, J. R. Li, H. C. Zhou, *J. Am. Chem. Soc.* **2016**, *138*, 6204.

[44] S. Yuan, Y. P. Chen, J. Qin, W. Lu, X. Wang, Q. Zhang, M. Bosch, T. F. Liu, X. Lian, H. C. Zhou, *Angew. Chem., Int. Ed.* **2015**, *54*, 14696.

[45] L. Huang, X. Zhang, Q. Wang, Y. Han, Y. Fang, S. Dong, *J. Am. Chem. Soc.* **2018**, *140*, 1142.

[46] D. Y. Chung, K. J. Lee, Y. E. Sung, *J. Phys. Chem. C* **2016**, *120*, 9028.

[47] T. Fujita, P. Guan, K. McKenna, X. Lang, A. Hirata, L. Zhang, T. Tokunaga, S. Arai, Y. Yamamoto, N. Tanaka, Y. Ishikawa, N. Asao, Y. Yamamoto, J. Erlebacher, M. Chen, *Nat. Mater.* **2012**, *11*, 775.

[48] M. Li, Z. Zhao, T. Cheng, A. Fortunelli, C. Y. Chen, R. Yu, Q. Zhang, L. Gu, B. V. Merinov, Z. Lin, E. Zhu, T. Yu, Q. Jia, J. Guo, L. Zhang, W. A. Goddard, Y. Huang, X. Duan, *Science* **2016**, *354*, 1414.

[49] A. Fortunelli, W. A. Goddard III, L. Sementa, G. Barcaro, F. R. Negreiros, A. Jaramillo-Botero, *Chem. Sci.* **2015**, *6*, 3915.